small structures
www.small-structures.com

# Niobium Oxide for Microplastics Degradation—the Effect of Crystal Structure and Morphology

*Atta Ur Rehman, Kang Ding Han, Muhammad Umair Ali, Yanling He, Aleksandr A. Sergeev, Zhengtian Yuan, Chunyang Dong, Xin Gao, Christelle A. Not, Alan Man Ching Ng, Kam Sing Wong, Zheng Xiao Guo, Ivor Lončarić, Jasminka Popović,* and Aleksandra B. Djurišić**

**Microplastic (MP) pollution is ubiquitous in the environment and there is a significant need for the development of photocatalysts for environmental remediation of microplastic pollution. Herein, the effect of the structure and morphology of $Nb_2O_5$ nanostructures on their photocatalytic activity for MP degradation is investigated. Nanostructures with a high fraction of pseudo-hexagonal TT-$Nb_2O_5$ phase are shown to effectively degrade pure polyethylene, polypropylene, and polyester, as well as MP samples collected from the environment. Efficient photocatalytic degradation of the microplastics is attributed to the unique structure and morphology (TT-$Nb_2O_5$ nanoparticles on monoclinic $Nb_2O_5$ rods), which facilitates charge separation and consequently photocatalytic activity. The $Nb_2O_5$ nanostructures with optimal composition and morphology lead to efficient degradation of not only pure plastic particles with different compositions (polyethylene, polypropylene, and polyester) in up to 64 h, but also complete degradation of environmental microplastics in 56 h.**

## 1. Introduction

There is a growing concern about environmental impact of microplastics (MPs) and their toxicity.[1–3] MPs, which are defined as plastic particles with sizes in the range from 1 μm to 5 mm, have been found to be widespread in the environment, including soil, water, and atmosphere.[1,2] MPs can have direct negative health impacts or act as a carrier for other pollutants.[2] While a number of regulatory measures have been implemented in different countries to limit the growth of plastic pollution by reducing plastic consumption,[1] there is a significant accumulation of plastic pollution in natural ecosystems.[2] As plastics are difficult to degrade by natural processes, resulting in the persistence of plastic pollution,[2] it is imperative to develop effective technologies to facilitate environmental remediation and removal/reprocessing of plastic waste. There are two possible approaches to eliminate MP pollution from the environment, namely mineralization to nontoxic chemicals ($CO_2$ and water) and upcycling into fuel and valorized chemicals.[3] Photocatalysis is particularly promising approach for environmental remediation of MPs, and it has been used for both mineralization of plastic wastes as well as photoreforming.[3–6] Consequently, photocatalysis for environmental remediation of plastic pollution has been

A. U. Rehman, M. U. Ali, Z. Yuan, A. B. Djurišić
Department of Physics
The University of Hong Kong
Pokfulam Road, Hong Kong, China
E-mail: dalek@hku.hk

K. D. Han
Department of Chemistry
National University of Singapore
21 Lower Kent Ridge Rd, Singapore 119077, Singapore

Y. He
Material characterization and preparation facility
The Hong Kong University of Science and Technology (Guangzhou)
No.1 Duxue Road, Guangzhou, Guangdong Province 511458, China

The ORCID identification number(s) for the author(s) of this article can be found under https://doi.org/10.1002/sstr.202500124.



**DOI: 10.1002/sstr.202500124**

A. A. Sergeev, K. S. Wong
Department of Physics
Hong Kong University of Science and Technology
Clear Water Bay, Kowloon, Hong Kong, China

C. Dong, X. Gao, Z. X. Guo
Department of Chemistry
The University of Hong Kong
Pokfulam Road, Hong Kong, China

C. A. Not
Department of Earth Science
The University of Hong Kong
Pokfulam Road, Hong Kong, China

A. M. C. Ng
Department of Physics and Core Research Facilities
Southern University of Science and Technology
Shenzhen 518055, China

I. Lončarić, J. Popović
Ruđer Bošković Institute
Bijenička 54, 10000 Zagreb, Croatia
E-mail: Jasminka.Popovic@irb.hr

extensively studied.[4–10] It should be noted that, while photoreforming to obtain useful chemicals from plastic waste is obviously of significant interest due to its potential for economic motivation for plastic waste removal, photocatalytic degradation under aerobic conditions by nonselective oxidation is still of significant interest as it converts toxic pollutants (MPs) into nontoxic product ($CO_2$) which could potentially be further processed separately. During photocatalytic degradation of MPs, photogenerated charge carriers react with water and oxygen to form reactive oxygen species (ROS), which together with photogenerated holes react with polymer chains, resulting in degradation to oligomers, monomers, and eventually $CO_2$.[4,5,9] Thus, one potential advantage of this process is its lack of selectivity—nonselective oxidation will degrade any type of organic compounds such as not only different plastics, which makes it particularly suitable for degradation of plastic pollution collected from the environment as these plastics may have accumulated other pollutants due to their tendency to adsorb and concentrate other pollutants present in the water.[8] Therefore, while photoreforming has the potential to be economically feasible, it would perform best on postconsumer sorted plastic waste which would not have a significant variation in the composition of starting chemicals. In contrast, MPs collected from the environment will exhibit compositional variations (i.e., types of plastics will likely vary depending on the area of collection), differences in adsorbed pollutants, and biofilms formed on the surface, etc. Consequently, due to compositional differences of environmental MPs, degradation as a nonselective oxidation process is expected to be more suitable for environmental remediation to ensure degradation of not only MP polymer but also any organic additives or adsorbed contaminants. In addition, photocatalytic degradation of MPs can be achieved not only in deionized water but also in lake and sea water, albeit at a lower degradation efficiency due to the presence of various ions.[11]

While promising results have been reported for plastics mineralization,[3–5] reports of complete mineralization of different plastics remain scarce and the time needed is frequently long (days or weeks), frequently under UV light rather than solar illumination.[4–6,9] The literature reports on photocatalytic plastic degradation are summarized in Table S1, Supporting Information. Long degradation times and incomplete degradation are particularly common for plastics with C—C backbones, such as polyethylene (PE) and polypropylene (PP), which are chemically inert and commonly take >100 h to degrade to more than 50%[5–7,12,13] or completely,[14] with very few exceptions demonstrating complete degradation of MPs,[12,14,15] or demonstrating ≥50%[16–18] or complete[15] degradation under visible illumination in less than 100 h. As PE and PP account for ≈57% of plastics produced, there is a clear need for the development of photocatalysts with simple scalable synthesis and improved photocatalytic performance for photocatalytic degradation of polyolefins.

Metal oxide-based photocatalysts have been commonly used for photocatalytic degradation of MPs,[5–7,11–27] with majority of the studies conducted on $TiO_2$ as a common photocatalyst, including $TiO_2$-based heterojunctions and doped $TiO_2$.[5–7,12–14,16–24] However, despite intensive research, there is still significant room for improvement, highlighting the need for the development of alternative material systems. For example, while complete degradation of plastics has been reported with $TiO_2$-based photocatalysts (Table S1, Supporting Information), this is typically achieved under UV illumination, while degradation rates under simulated solar illumination are typically significantly lower. In contrast, $Nb_2O_5$ has been shown to degrade plastics under solar illumination,[15] which makes it a promising candidate for photocatalytic applications. In general, niobium oxide is particularly interesting among various metal oxides, as it is a nontoxic oxide with a significant oxidation ability and Lewis and Brønsted acid sites on surface which are located at tetrahedral $NbO_4$ and octahedral $NbO_6$ units, respectively.[28] Consequently, it is of interest for photocatalytic applications.[28,29] Part of the interest in $Nb_2O_5$ is the fact that it can crystallize in a variety of crystal structures, including hexagonal $Nb_2O_5$, pseudo-hexagonal phase TT-$Nb_2O_5$, orthorhombic phase T-$Nb_2O_5$, tetragonal *M*-$Nb_2O_5$, and monoclinic phase H-$Nb_2O_5$.[28,29] In addition, a variety of nanostructured morphologies, including particles, rods, and plates can be readily synthesized.[28] Various photocatalytic applications of $Nb_2O_5$[15,28–39] have been demonstrated to date, including $H_2$ production,[28,30,31] $CO_2$ reduction,[28] selective transformation of amine and alcohols,[28] and the degradation of pollutants[28,33,35,36] including plastic degradation and reforming.[15]

For plastic degradation, orthorhombic single unit cell thick $Nb_2O_5$ layers (JCPDS card No. 27-1003) have been shown to be very effective in degrading different plastics under simulated solar irradiation, including PE and PP.[15] $Nb_2O_5$ layers could degrade not only pure plastics purchased from a supplier, but also single-use bags, food containers, and food wrap film, and the degradation produced not only $CO_2$ but also $C_2$ fuels although at a low yield.[15] However, other photocatalytic applications of $Nb_2O_5$ have found different optimal crystal structures for photocatalytic activity. For example, TT-$Nb_2O_5$ was found to be the most active phase for hydrogen evolution,[28] but efficient hydrogen evolution was also reported for monoclinic rods[30] and TT/T pseudohexagonal/orthorhombic heterophase junctions.[31] Similarly, for pollutant degradation hexagonal phase,[35] monoclinic phase[38] and pseudo-hexagonal [TT] phase[33] were found to be superior to the orthorhombic phase. Consequently, the relationship between crystal structure and photocatalytic activity of $Nb_2O_5$ is still not fully clear.

Thus, here we investigated the influence of the crystal structure and morphology of $Nb_2O_5$ nanostructures for the photocatalytic degradation of microplastics. We have varied the synthesis conditions to obtain different fractions of various crystal phases (TT-$Nb_2O_5$ and monoclinic phases) and morphologies (nanoparticles, rods, large particles), and we investigated their application to photocatalytic degradation of MPs. We have used PE as the model MPs, since PE is a common plastic material with C—C backbone which is difficult to degrade due to its chemical stability.[4] We have found that samples with a high fraction of pseudo-hexagonal TT-$Nb_2O_5$ phase exhibit high photocatalytic activity, resulting in complete degradation of different MPs (PE, PP, and polyester (PES)) in 56–64 h depending on the type of plastics.

## 2. Results and Discussion

Different from common practices to obtain different $Nb_2O_5$ phases by varying annealing temperature,[32,34] we prepared

$Nb_2O_5$ nanostructures using different amounts of water added during the synthesis to vary the structure and morphology of the samples, while the same low annealing temperature (250 °C) was used for all the samples. The amount of water added during the synthesis was systematically varied in order to obtain samples with different crystal structures, as the addition of water yielded an appearance of a new crystal phase not obtained in the samples prepared without water, while the amount of water added controlled the ratios of the phases present. We have then tested the photocatalytic activity of prepared samples for degradation of microplastics by measuring the mass loss of MPs[4,6,11] as a function of illumination time. The size distributions and SEM images of PE and PP MPs are shown in Figure S1 and S2, Supporting Information, respectively. PES fibers and environmental plastics were subjected to ball milling to obtain fragments with ≈2 μm size, as described in our previous work.[14] We can observe that $Nb_2O_5$ (prepared with 0 mL water) can degrade all the investigated samples, as shown in **Figure 1**a. Degradation times for complete mass loss are similar for all three types of plastics (PE, PP, and PES fibers). While PES is expected to be more susceptible to photodegradation compared to PE and PP polymers with stable C—C backbones, it has unfavorable morphology (long fibers) and requires ball milling for efficient degradation.[14] The plastic degradation rate is dependent on the ratio of photocatalyst and PE MPs, with slower degradation occurring for lower $Nb_2O_5$:MP ratio, as shown in Figure S3, Supporting Information. It should be noted, however, that a practical application of photocatalytic degradation of MPs should include optimization of reaction conditions, as well as the reactor design. For the purpose of investigating the effect of photocatalyst properties on photocatalytic activity, comparisons need to be done under the same reaction conditions. While higher photocatalyst to MP ratios are less economically attractive, they allow faster completion of the experiments and hence further experiments were performed at higher $Nb_2O_5$:MP ratio used in experiments in Figure 1a. In addition, the reproducibility of degradation was tested across different batches of $Nb_2O_5$ nanostructures, and excellent reproducibility is obtained, as shown in Figure S4, Supporting Information. While different batches showed variations in the ratios of different crystal phases (Figure S5, Supporting Information and **Figure 2**a), similar degradation curves are obtained for samples (Figure S4a, Supporting Information). Next, to investigate the effect of crystal structure of the samples across wider range of possible structures, we tested photocatalytic activity for degradation of PE MPs as a commonly used model plastics for $Nb_2O_5$ nanostructure prepared with different amounts of $H_2O$, and the obtained results are shown in Figure 1b. We can observe efficient degradation of PE for the sample with 0 mL water added during the synthesis, followed by the sample with 0.5 mL. In the case of 1 mL sample, significantly slower degradation is observed, while the 3 mL sample exhibits negligible photocatalytic activity. The evolved gases during the degradation of PE were determined by gas chromatography (GC), and obtained results are shown in Figure 1c. Similar to previous studies, $CO_2$ is the main degradation product,[12,15] with a small amount of CO[12,15] also present.

To investigate the reasons for the differences in photocatalytic activity, comprehensive characterization of the obtained samples is performed. As $Nb_2O_5$ is known to crystallize in a variety of structures depending on the synthesis conditions,[28,29,39–44] XRD measurements were performed, and the results of Rietveld refinement are shown in Figure 2.

Quantitative analysis revealed that crystallization of different $Nb_2O_5$ phases strongly depends on the amount of water during the synthesis. We can observe that sample prepared without water dominantly contain hexagonal phase, in literature commonly denoted as TT-$Nb_2O_5$. However, the structure of TT polymorph, often also referred to as "pseudo-hexagonal" phase, was vastly discussed in the literature but no space group has been assigned until just recently.[39] Our refinements show that TT-$Nb_2O_5$ crystallize in the P6/*mmm* space group with refined unit-cell parameters $a = 3.6101(5)$ Å and $c = 3.9478(8)$ Å, confirming the structure as obtained by Košutova et al.[39] It is important to notice that TT polymorph is, in fact, an oxygen-deficient nonstochiometric structure with O/Nb ratio ≈2.2 (the O/Nb ratio in stoichiometric $Nb_2O_5$ is 2.5). The sample prepared without water also contains C2/*m* monoclinic phase, denoted monoclinic phase I, with the refined unit cell parameters $a = 12.7704(6)$, $b = 3.8404(6)$ Å, and $c = 3.9874(1)$ Å, $\beta = 91.6°$. The structure published by Gruehn[40] was used as the structural model for refinement. It should be noted that this phase is rarely found isolated, and it commonly occurs in mixtures with other polymorphs.[44] As the amount of water increases, we observe that the amount of hexagonal TT phase decreases, which is also

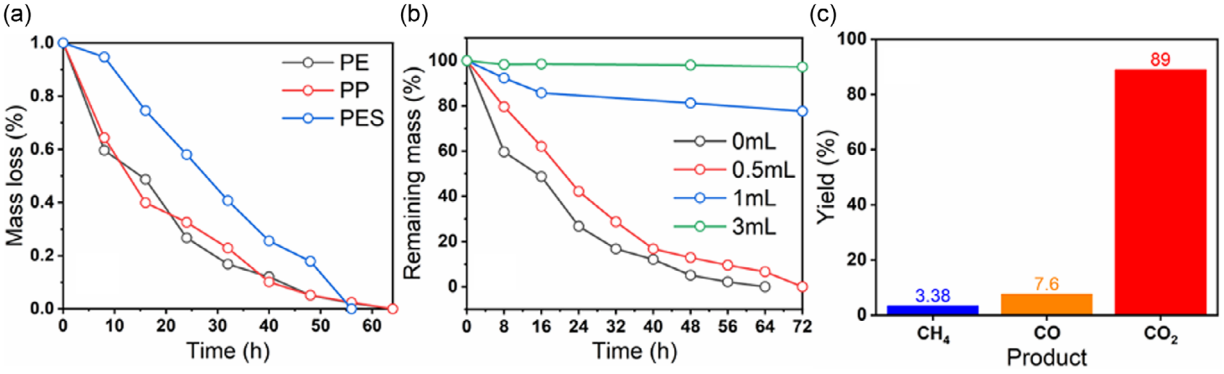


**Figure 1.** a) Remaining mass of PE, PP, and PES for $Nb_2O_5$ nanostructures prepared with 0 mL $H_2O$. b) Remaining mass of PE as a function of simulated solar illumination time for $Nb_2O_5$ nanostructures prepared with different amounts of $H_2O$. c) Percentages of evolved gases detected by GC.

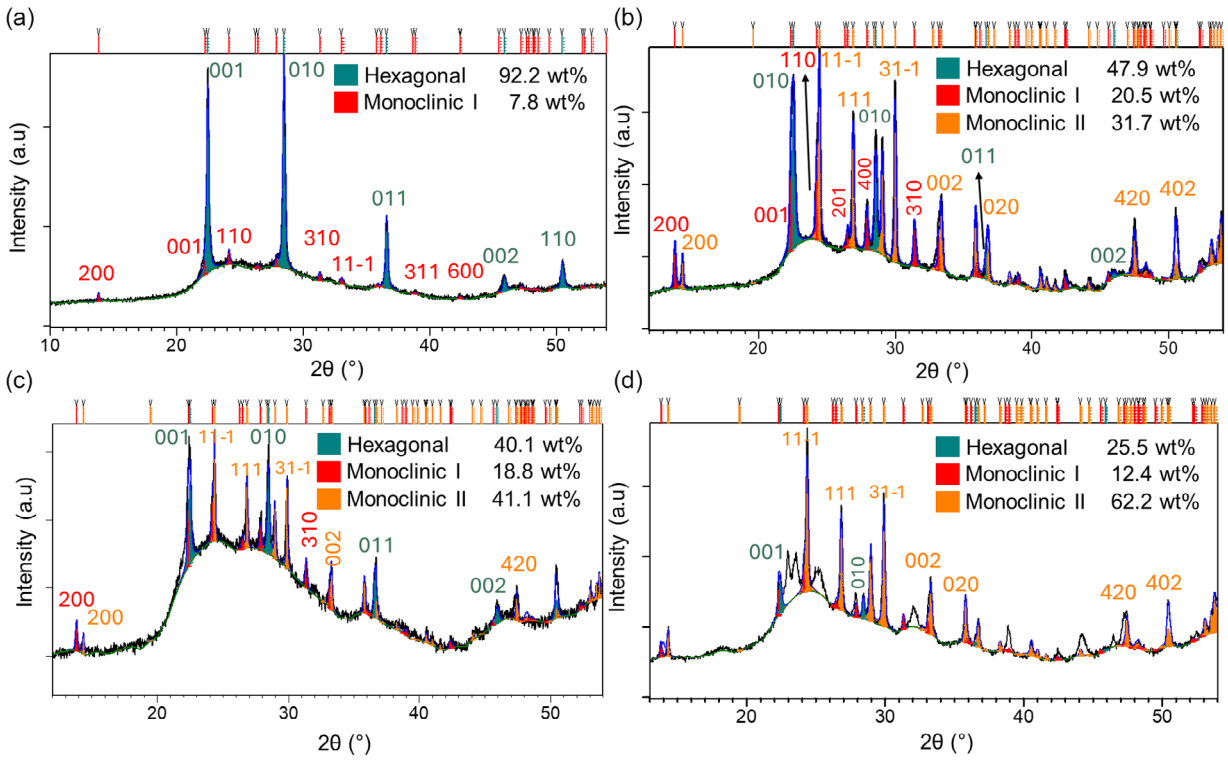


**Figure 2.** XRD patterns of $Nb_2O_5$ nanostructures prepared with a) 0 mL, b) 0.5 mL, c) 1 mL, and d) 3 mL $H_2O$. Experimental data are shown by black line, calculated pattern by blue line while the vertical teal, red, and orange lines represent hexagonal and monoclinic phases, respectively.

accompanied by the crystallization of the second distinct monoclinic phase. Monoclinic phase II belongs to the C2/*c* space group with the refined unit cell parameters $a = 12.7410(7)$, $b = 4.8865(7)$ Å, and $c = 5.5633(5)$ Å, $\beta = 105.1°$, which corresponds to the structure published by Ercit.[41] We can observe that samples prepared with increasing amount of $H_2O$ contain increasing fraction of monoclinic phases, mainly due to monoclinic II phase which is absent for 0 mL sample and its fraction increases with increasing amount of water at the expense of both TT and, for water containing samples, monoclinic I phases. Considering that monoclinic $Nb_2O_5$ were previously synthesized by a hydrothermal process,[30] it is not surprising that the addition of water during the synthesis could increase the fraction of monoclinic polymorphs. Thus, from XRD analysis, it is obvious that all the samples contain multiple crystal phases. The presence of multiple phases in the samples can be an advantage for photocatalytic applications, since the existence of heterophase junctions can facilitate charge carrier separation and consequently photocatalytic activity,[31] and thus photocatalysts exhibiting a mixture of phases can exhibit higher photocatalytic activity compared to pure phase samples.[34]

Additionally, we have investigated the morphology of the prepared samples by transmission electron microscopy (TEM), high-resolution transmission electron microscopy (HRTEM), and selected area electron diffraction (SAED), as shown in **Figure 3**. TEM images for all samples show two distinct morphologies, namely rods and nanoparticles. Additional TEM images at different magnification levels are shown in Figure S6, Supporting Information, since the significant size disparity between small nanoparticles and larger rods makes it difficult to clearly observe both types of morphologies at the same magnification level. Due to very small size (<20 nm) of commonly found nanoparticles, HRTEM images shown in Figure 3 (panels c) are most suitable for observing this morphology.

The *d*-values, obtained from HRTEM and SAED images of rods in the case of the sample prepared without water, amount to 0.282 nm and 0.370 nm which correspond to $hkl = 310$ and $hkl = 201$ of monoclinic I phase, respectively. In the case of sample prepared with 0.5 mL of water, *d* value that amounts to 0.2653 nm is also observed for rods which is attributed to $hkl = 002$ of monoclinic phase II. While *d* values characteristic for monoclinic $Nb_2O_5$ polymorphs are observed in rods in all samples, nanoparticles are exhibiting *d* values that are attributed to the hexagonal $Nb_2O_5$; typically $d = 0.313$ nm that corresponds to $hkl = 010$ and $d = 0.164$ nm that is attributed to $hkl = 111$. Thus, the samples exhibit distinct differences in composition (different polymorphs present), as well as morphology. In samples exhibiting significant photocatalytic activity, namely 0–0.5 mL, we can observe that they consist of larger rods and nanoparticles which are in close contact with the rods, which could possibly play a role in charge separation. For 1 mL samples, there is more separation between the rods and nanoparticles, while 3 mL sample appears to be a more disordered mixture of larger structures and nanoparticles. Thus, differences in photocatalytic activity could originate from crystal structure differences, morphology differences, or their combined effects.

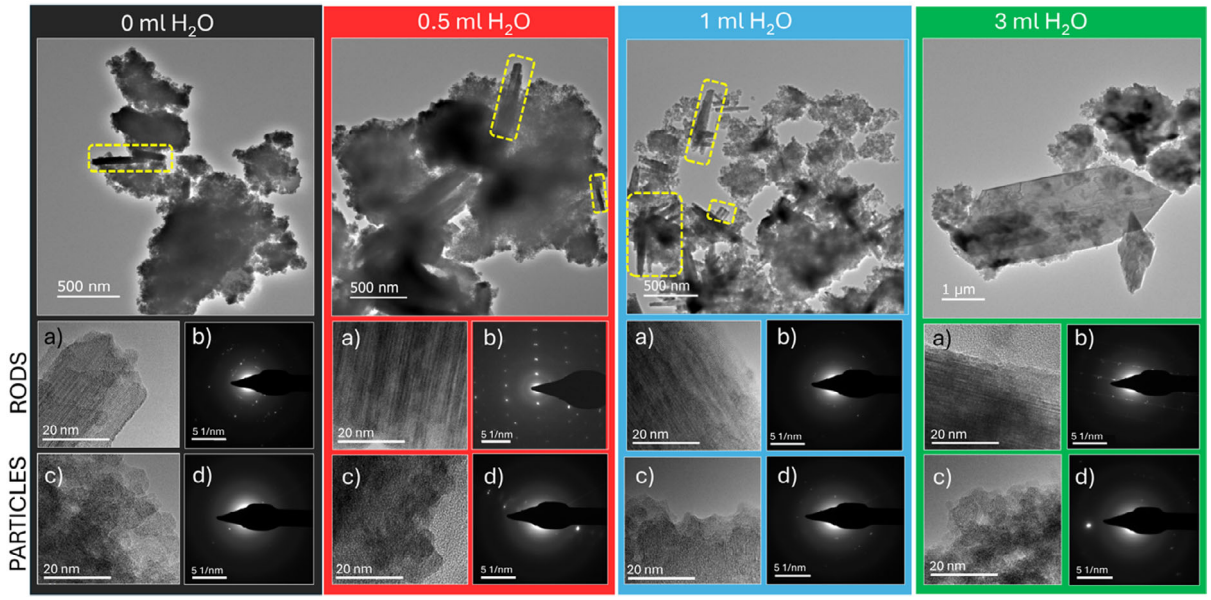


**Figure 3.** Representative electron microscopy and diffraction images of $Nb_2O_5$ nanostructures prepared with 0, 0.5, 1, and 3 mL $H_2O$ are given in dark gray, red, blue, and green panels, respectively. First row in each panel shows TEM images. Rods are highlighted with yellow dashed lines. a,c) HRTEM images and b,d) corresponding SAED images for two present morphologies: rods (second row) and nanoparticles (third row).

To further investigate the role of differences between the samples, additional characterization of their composition and optical properties was performed. As the photocatalytic activity of $Nb_2O_5$ is known to be affected by native defects, in particular oxygen vacancies,[28,32] we performed Fourier transform infrared spectroscopy (FTIR) and X-ray photoelectron spectroscopy (XPS) characterization, and the obtained results are shown in Figure S7, Supporting Information. In the XPS spectrum of O1s, lower energy peak at (≈529.7–531.7 eV) can be attributed to lattice oxygen, while the higher energy peak (≈532–533 eV) can be attributed to surface oxygen and/or oxygen vacancies.[29,32,37,38] We can observe that samples exhibiting more pronounced higher energy peak in the XPS O 1s spectrum, namely 0 mL and 3 mL, also exhibit more pronounced peak in the region 3000–3600 $cm^{-1}$ which can be attributed to hydroxyl group vibrations,[41] and thus, we can attribute this feature to surface oxygen. However, there is no obvious relationship between surface hydroxyl groups and photocatalytic activity of the samples. Therefore, we examined the optical properties of the samples. Absorption spectra and sample photos are shown in Figure S8. We can observe that the absorption of the samples is consistent with the $Nb_2O_5$ bandgap, which is in the range ≈3.0–3.4 eV.[28] However, in this case as well there is no clear relationship between the optical properties and photocatalytic activity, which is contrary to the expectation that the sample exhibiting higher absorption in the visible spectral range would exhibit the highest photocatalytic activity.[32] The sample exhibiting the best photocatalytic activity, 0 mL, was pale yellow color and exhibited the lowest absorption in the visible spectral range. The 0.5–1 mL samples exhibited more significant absorption in the visible spectral range. As they exhibit lower photocatalytic activity under simulated solar illumination compared to 0 mL sample despite higher absorption, this indicates higher recombination losses in these samples. To examine charge carrier dynamics, time-resolved photoluminescence (TRPL) measurements were performed, and obtained results are shown in Figure S2b, Supporting Information.

We can observe the fastest decay of luminescence in 0 mL samples. This could possibly indicate either higher nonrecombination losses, which are not consistent with the observed high photocatalytic activity, or improved charge separation. It is known that niobium oxide heterophase junctions can exhibit efficient charge separation and consequently high photocatalytic activity, as demonstrated for TT-$Nb_2O_5$/T-$Nb_2O_5$ junctions for photocatalytic hydrogen evolution.[31] Charge transfer between different crystal phases is also responsible for high photocatalytic activity of model P25 photocatalyst, which consists of a mixture of anatase and rutile phases of $TiO_2$.[37] We can observe that while 0 mL samples and 3 mL samples exhibit similar absorption and presence of surface oxygen, they exhibit significantly different TRPL curves, indicating differences in photogenerated charge dynamics. Those differences can occur due to morphological differences, that is, lack of close contact between particles and rods, preventing the formation of heterophase junctions and charge separation. Alternatively, the crystal structure differences, that is, the presence of different phases can also affect charge transfer. For example, samples 0–0.5 mL have similar morphologies, but significantly different optical properties, and sample 0.5 mL exhibits lower photocatalytic activity and slower TRPL decay compared to 0 mL sample. One possible explanation is that both TT-$Nb_2O_5$ and monoclinic II crystal phases have wider bandgap compared to monoclinic I phase, which is consistent with lower visible light absorption in 0–3 mL samples which have lower content of monoclinic I phase. The photocatalytic activity of the samples is directly correlated to the content of photocatalytically active TT-$Nb_2O_5$ phase, while the presence of monoclinic II

phase is detrimental to photocatalytic activity of the samples, as it changes charge carrier dynamics and consequently reduces photocatalytic activity.

To obtain further insight into charge dynamics in the samples, transient absorption (TA) measurements were conducted, and the obtained results are shown in **Figure 4** and Figure S9, Supporting Information. As the samples exhibit significant scattering, the sharp-peak feature present in all samples at ≈500 nm, likely originating from slight beam deviation caused by delay stage movement, is an experimental artifact and should be ignored. We can also observe that there is no TA signal in the range 360–400 nm for all the samples, consistent with the fact that $Nb_2O_5$ is a wide bandgap semiconductor (360 nm corresponds to ≈3.4 eV). Thus, no ground-state bleaching corresponding to valence band (VB) to conduction band (CB) transition is observed, and two distinct bands in the visible spectra range at ≈450–700 nm can be assigned to trap-induced bleaching. These two levels at ≈450–700 nm are labeled as "2.75 eV" and "1.77 eV," respectively, in a schematic diagram in **Figure 5**a. We can observe that the signal corresponding to higher energy defect state at ≈450 nm decreases with decreasing content of the TT-$Nb_2O_5$ phase, and the increase in the monoclinic II phase results in the ≈700 nm band increase. No direct transfer between these two defect states is observed. From the tail (100–1000 ps) of TA kinetics measured at 440–480 nm (Figure S9c, Supporting Information), we can observe behavior consistent with TRPL in the range of 100–1000 ps, with the fastest decay obtained for 0 mL sample, while no significant differences are observed in the kinetics of ≈700 nm band. (Figure S9d, Supporting Information). To gain more insight into the role of different phases in charge carrier dynamics, electronic structure of all three phases was calculated with density functional theory (DFT) and obtained results are shown in Figure 5b–d. We can observe that pseudohexagonal TT-$Nb_2O_5$ phase in our calculations has slightly doped conduction band, different from semiconducting monoclinic phases. Occupation of conducting band of TT-$Nb_2O_5$ is not unexpected, since this crystal structure is considered to be stabilized by impurities (OH, Cl) and oxygen vacancies,[43,44] and in our calculations, we have used idealized structure with formula $Nb_4O_9$.

From the obtained TA results, we conclude that the population of two defect bands ("2.75 eV" and "1.77 eV" in Figure 5a) is strongly dependent on the sample composition, with decrease in TT-$Nb_2O_5$ content and an increase in monoclinic II phase content resulting in decreased population of level "2.75 eV" and increased population of level "1.77 eV" band. Due to low energy

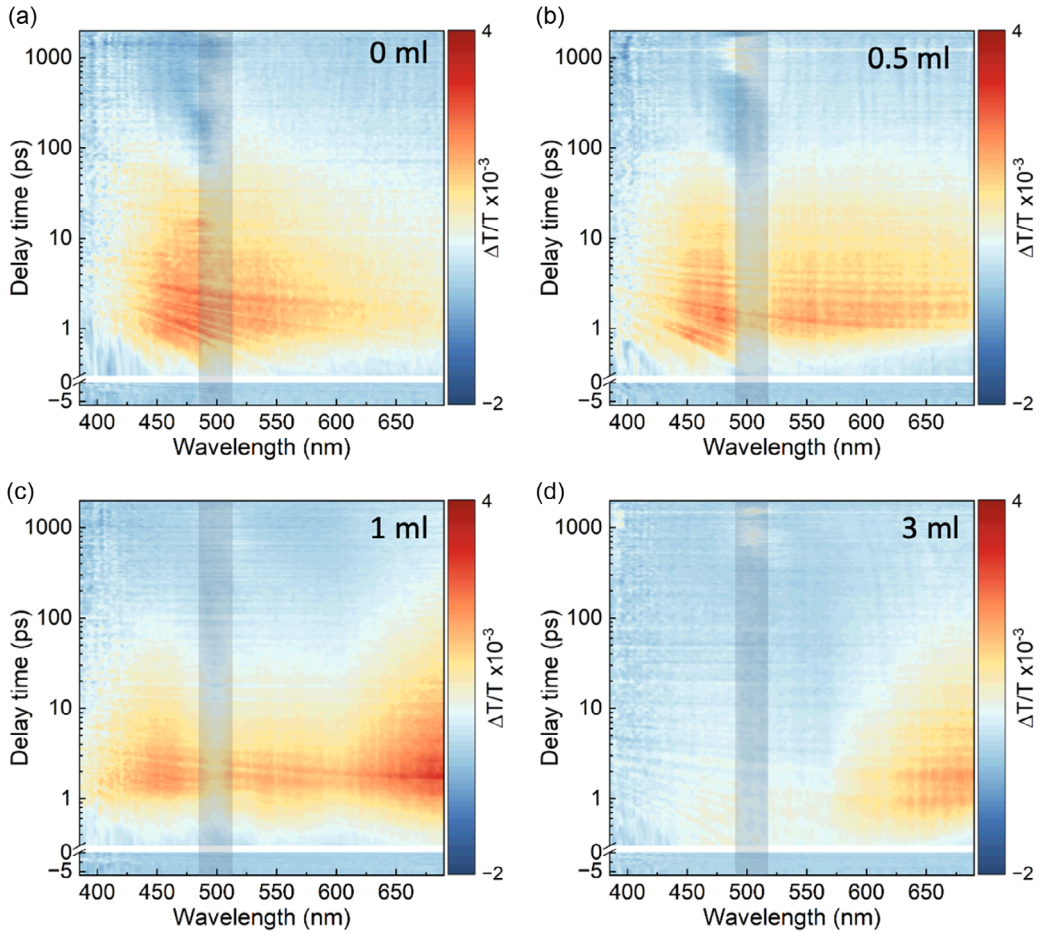


**Figure 4.** Transient absorption spectra of $Nb_2O_5$ films prepared from $Nb_2O_5$ nanostructures synthesized with different amounts of water a) 0 mL, b) 0.5 mL, c) 1 mL, and d) 3 mL.

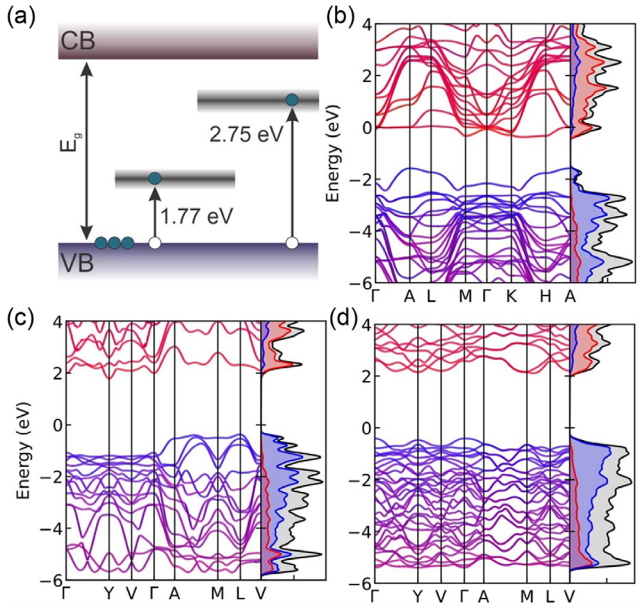


**Figure 5.** a) Schematic diagram of the transient absorption processes involving defect states. Band structure and projected density of states for b) TT-$Nb_2O_5$, c) Monoclinic I, and d) Monoclinic II. Energy of 0 eV corresponds to the Fermi level.

of 1.77 eV nm band, charge carriers trapped at this level likely cannot participate in the redox reactions involved in photocatalytic degradation of MPs. As we know that TT-$Nb_2O_5$ phase contains significant states in the gap (Figure 5b), and from TA results defect states can be directly populated by absorption of low-energy photons. As the ≈450 nm correlates well with TT-$Nb_2O_5$ phase content and photocatalytic activity, we can conclude that the 2.75 eV band likely originates from TT-$Nb_2O_5$ and it is responsible for photocatalytic degradation of microplastics under simulated solar illumination. In contrast, 1.77 eV band is photocatalytically inactive, and it can originate either from defect states in monoclinic II phase, or charge transfer across the heterophase junction.

As the photocatalytic degradation of microplastics involves oxidative cleavage of C—C bonds,[15] a number of possible reactions occur, involving the generation of different radical species, and ultimately ending in the production of $CO_2$. The degradation reactions for photocatalytic degradation of PE proposed in the literature are summarized in Equation (1–14).[15,45,46]

$$H_2O + h^+ \rightarrow {}^{\bullet}OH + H^+ \quad (1)$$

$$O_2 + e^- \rightarrow O_2^{\bullet-} \quad (2)$$

$$O_2^{\bullet-} + e^- + 2H^+ \rightarrow H_2O_2 \quad (3)$$

$$H_2O_2 + 2e^- + 2H^+ \rightarrow 2H_2O \quad (4)$$

$$O_2^{\bullet-} + H_2O \rightarrow {}^{\bullet}HO_2 + OH^- \quad (5)$$

$$O\,H^- + h^- \rightarrow {}^{\bullet}OH \quad (6)$$

$$(-CH_2 - CH_2-)_n + {}^{\bullet}OH \rightarrow (-{}^{\bullet}CH - CH_2-)_n + H_2O \quad (7)$$

$$(-{}^{\bullet}CH_2 - CH_2-)_n + O_2 \rightarrow (-CH_2 - {}^{\bullet}HCOO - CH_2-)_n \quad (8)$$

$$(-CH_2 - {}^{\bullet}HCOO - CH_2-)_n + (CH_2 - CH_2-)_n \rightarrow (-CH_2 - HCOOH - CH_2-)_n + (-{}^{\bullet}CH - CH_2-)_n \quad (9)$$

$$(-CH_2 - HCOOH - CH_2-)_n \rightarrow (-CH_2 - {}^{\bullet}HCOO - CH_2-)_n + H^+ \quad (10)$$

$$(-CH_2 - HCOOH - CH_2-)_n \rightarrow (-CH_2 - {}^{\bullet}HCO - CH_2-)_n + {}^{\bullet}OH \quad (11)$$

$$(CO_2 + e^- + H^+ \rightarrow {}^{\bullet}COOH) \quad (12)$$

$$({}^{\bullet}COOH + e^- + H^+ \rightarrow CO + H_2O) \quad (13)$$

$$(-CH_2 - CH_2-)_n \xrightarrow{{}^{\bullet}OH,\,O_2} 2nCO_2 \quad (14)$$

Therefore, as the first step in the degradation of PE involves the production of reactive oxygen species (Equation (1–6)) which requires favorable energy level alignment between photocatalyst and redox potentials of the reactions involved,[15] it is not unexpected that the excitation of lower energy state (1.77 eV) would

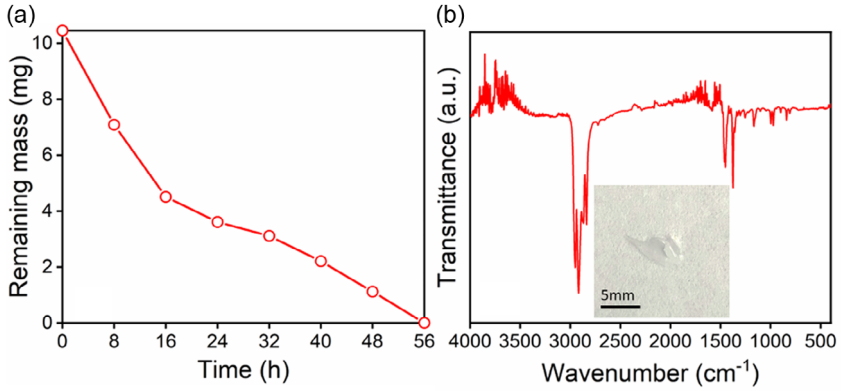


**Figure 6.** a) Remaining mass of environmental plastics as a function of simulated solar illumination time for $Nb_2O_5$ nanostructures prepared with 0 mL $H_2O$. b) FTIR spectrum of the environmental plastic sample. Inset shows photo of the sample.

not result in high production of reactive oxygen species and consequently would yield poor photocatalytic activity.

Finally, we have applied the best-performing sample (0 mL) to the photocatalytic degradation of environmental MPs, which were collected from marine environment. The environmental MP sample was identified to be weathered PP, as shown in **Figure 6**, as the measured FTIR peaks correspond well to characteristic peaks of PP due to C—H and C—C vibrations at ≈2951 $cm^{-1}$, 2918 $cm^{-1}$, 2867 $cm^{-1}$, 2837 $cm^{-1}$, 1454 $cm^{-1}$, 1375 $cm^{-1}$, 1167 $cm^{-1}$, 997 $cm^{-1}$, and 973 $cm^{-1}$.[20] As PP MPs are one of the major MP pollutants in aquatic systems,[8,16] due to their high production rate, common use in packaging, as well as protective equipment during the pandemic,[16] it is expected to find PP pieces among environmental MP samples. We can observe that environmental MPs can be efficiently degraded by $Nb_2O_5$ photocatalyst in 56 h. Faster degradation compared to pure PP (Figure 1a) can occur due to differences in particle size as well as weathered surface of environmental MPs, which offers additional sites for oxidative attack leading to photocatalytic degradation.

## 3. Conclusion

We have prepared $Nb_2O_5$ nanostructures with different crystal structures and investigated their photocatalytic activity for microplastic degradation. The high content of TT-$Nb_2O_5$ phase was associated with high photocatalytic activity, and photocatalytic activity decreased with increasing content of monoclinic phase II with C2/*c* space group which occurred concurrently with the reduction of TT-$Nb_2O_5$ content. The decrease in photocatalytic activity with the increasing content of monoclinic phase II with C2/*c* space group can be attributed to a decrease in population of higher energy defect states (≈2.75 eV) and an increase in population of lower energy defect states (≈1.77 eV) which do not contribute to photocatalytic plastics degradation. The samples with the highest photocatalytic activity predominantly consist of TT-$Nb_2O_5$ nanoparticles in close contact with nanorods with C2/*m* monoclinic phase, which likely facilitates charge separation. For samples with optimal composition, complete degradation of pure microplastics samples (PE, PP) and environmental microplastics samples (PP) could be achieved under simulated solar illumination within 56–64 h. This makes $Nb_2O_5$ a promising candidate for photocatalytic environmental remediation of microplastics pollution.

## 4. Experimental Section

*Materials*: Niobium chloride ($NbCl_5 \geq 99.9\%$, metal basis) was purchased from Aladdin Scientific. Benzyl alcohol (99%), PE, and PP were purchased from Henan Alfa Chemicals, China. PES was obtained from Dingwang Co., Ltd. Environmental plastic samples were collected from a water source in Tsing Lung Tau (22.35713, 114.03479), situated on the southwest coast of the New Territories in Hong Kong, as previously described.[14,47,48] No shape or polymer sorting was conducted prior to the degradation process. Environmental samples and PES samples were ground into particles ≈2 μm in size using a ball mill (Retsch, PM400) to facilitate degradation.[14]

*Photocatalyst Synthesis*: 600 mg of $NbCl_5$ was added into 60 mL of benzyl alcohol, and the mixture was subjected to sonication until complete dissolution of $NbCl_5$, resulting in a yellowish solution. Subsequently, varying volumes of water (0, 0.5, 1, or 3 mL) were added to the solution, followed by further sonication. The prepared mixture was then transferred to a 100 mL Teflon-lined autoclave and heated in a muffle furnace at 250 °C for 3 days. The resultant gel-like product was transferred into centrifuge tubes and repeatedly washed with acetone. The precipitates were dried in a vacuum oven at 70 °C overnight and then ground into a fine powder for subsequent characterization and testing.

*Characterization*: The XPS spectra of O 1s were obtained using a PHI VersaProbe 4, with a pass energy of 112 eV and an energy resolution of 0.1 eV. The FTIR measurements were conducted using a Vertex 70 V spectrometer. Before measurement, KBr powders were baked under vacuum at 12 °C for 12 h for further use. The concentration of $Nb_2O_5$ in KBr is 1% by weight. One milligram of $Nb_2O_5$ powder was mixed with 100 mg of KBr powder and pressed for 60 s to form a pellet for measurement. The FTIR analysis of polypropylene was conducted using a Vertex 70 V (Bruker) in attenuated total reflectance mode. The sample was measured without any pretreatment, as collected. HRTEM and SAED were performed using an FEI F30 at 300 kV. $Nb_2O_5$ powder samples were added to ethanol, and the mixture was uniformly dispersed to form a suspension using ultrasound for 30 min. The suspension was deposited onto copper grids and dried under vacuum for 1 h for measurement. Ultraviolet absorption (UV-vis) spectra were obtained using an Agilent Cary 60 UV-Vis spectrometer (Agilent Technologies, USA). Photoluminescence (PL) spectra were acquired with an FLS1000 Photoluminescence Spectrometer (Edinburgh Instruments Ltd., UK) employing Xenon lamp excitation at 325 nm, while a 375 nm laser diode was used as the excitation source for time-resolved PL (TRPL) measurements on the same equipment. Transient absorption (TA) measurements were performed on spin-coated $Nb_2O_5$ films on quartz substrates (spin coating at 1000 rpm from a water suspension of $Nb_2O_5$ powder at a concentration of 20 mg $ml^{-1}$). TA was performed using a home-built setup comprising a femtosecond laser source (Coherent Legend) and an optical parameter amplifier (OPA, OperaSolo). The fundamental emission from the laser had a center wavelength of 800 nm, pulse duration of ≈100 fs, and a repetition rate of 1 kHz. The laser beam was split into two, with one beam directed into the OPA to generate the pump pulse which was centered at 300 nm with an intensity of 25 μJ $cm^{-2}$ and frequency chopped at 500 Hz. The other part was used to generate a broadband continuum light in 350–700 nm range as the probe beam. A motorized stage was used in the optical path of the probe beam to achieve up to 1 ns time delay with femtosecond resolution. The probe beam was focused on the sample using a 150 mm lens at a normal incidence angle, resulting in a 150 μm spot size as measured by an optics-free CCD. The pump beam was directed onto the sample at an angle of 10° from the normal incidence. To ensure sufficient spatial overlap with the probe beam, the pump beam diameter was set to 1.5 mm via a pinhole. The differential transmission spectrum of the probe pulse (ΔT/T) was calculated as $((T_{pump}\ ON - T_{pump}\ OFF)/T_{pump}\ OFF)$. Shot-by-shot transmission of the probe beam was collected by an Acton Spectrapro 275 spectrometer equipped with a 150 ln $mm^{-1}$ grating and a silicon line CCD. The instrumental response function was 150 fs.

*Calculations*: Starting points for calculations were the XRD crystal structures for different polymorphs. For TT-$Nb_2O_5$, we have constructed $2 \times 2 \times 1$ supercell and removed one oxygen atom with partial occupancy to obtain ratio O/Nb of 2.25, similar to the experimental one.

The density functional theory (DFT) calculations of electronic structure of $Nb_2O_5$ were carried out with the VASP code. The Perdew–Burke–Ernzerhof (PBE) approximation was adopted to describe the exchange and correlation functional. An energy cutoff of 520 eV was used for the plane wave basis set. The atomic positions were optimized using a convergence threshold of $10^{-5}$ eV for energy between two ionic steps.

*Photocatalytic Degradation of Microplastics*: A mixture of 50 mg of catalyst and 10 mg of microplastic was dispersed in a 25 mL beaker containing 10 mL of deionized water. The mixture was sonicated under simulated solar illumination (1 Sun, AM 1.5 G). The degradation of the plastics was assessed by measuring mass loss over fixed time intervals, which is a commonly used method for determining plastic degradation. However, using filter paper to separate microplastics from the solution

can introduce errors and uncertainties due to the adhesion of micro/nanoparticles to the filter paper. To avoid this issue, the initial mass of the microplastic ($M_0$), the initial mass of the photocatalyst ($M_{pc}$), and the mass of the beaker ($M_b$) were measured. After each interval, the sample was dried in a vacuum oven at 70 °C, cooled to room temperature, and the total mass ($M_T$) was measured. The mass loss of the plastic ($\Delta M$) was then calculated as $\Delta M = (M_0 + M_{pc} + M_b) - M_T$. Mass measurements were conducted using a Mettler Toledo XSR105 balance with a hanging mass pan, ensuring high stability and exceptional repeatability. To collect the gaseous products from the photocatalytic conversion of polyethylene (PE), the reaction was conducted in a closed system using a multichannel photoreactor (Photosyn-10, Shanghai Quanhuan Technology Co., Ltd.). Specifically, 20 mg of catalyst, 10 mg of microplastics (MPs), and 5 mL of $H_2O$ were added to a 25 mL quartz tube. The mixture underwent ultrasonication for 10 min, followed by stirring under 365–800 nm solar light at room temperature for 24 h. The gaseous products were collected using a 20 mL syringe and then transferred to an aluminum foil gas bag. The gas samples were manually transferred from the gas bag to a GC system (Agilent 8860) equipped with both a thermal conductivity detector and a flame ionization detector for analysis. The gaseous products were identified by matching their retention times with reference standards and quantified by analyzing the area under the curve using a pre-established calibration curve.

## Supporting Information

Supporting Information is available from the Wiley Online Library or from the author.

## Acknowledgements

This work was funded by the Environment and Conservation Fund (ECF Project No. 141/2021). Any opinions, findings, conclusions, or recommendations expressed in this material/event do not necessarily reflect the views of the Government of the Hong Kong Special Administrative Region and the Environment and Conservation Fund.

## Conflict of Interest

The authors declare no conflict of interest.

## Author Contributions

**Atta Ur Rehman**: investigation (lead); visualization (lead). **Kang Ding Han**: investigation (supporting). **Muhammad Umair Ali**: investigation (supporting). **Yanling He**: investigation (supporting); visualization (supporting). **Aleksandr A. Sergeev**: investigation (supporting); visualization (supporting); writing—original draft (supporting). **Zhengtian Yuan**: investigation (supporting). **Chunyang Dong**: investigation (supporting). **Xin Gao**: investigation (supporting). **Christelle A. Not**: resources (supporting); writing—review and editing (supporting). **Alan Man Ching Ng**: funding acquisition (supporting); writing—review and editing (supporting). **Kam Sing Wong**: writing—review and editing (supporting). **Zheng Xiao Guo**: funding acquisition (supporting); writing—review and editing (supporting). **Ivor Lončarić**: investigation (supporting); visualization (supporting). **Jasminka Popović**: formal analysis (equal); investigation (supporting); visualization (supporting); writing—original draft (supporting); writing—review and editing (supporting). **Aleksandra B. Djurišić**: conceptualization (lead); funding acquisition (lead); project administration (lead); writing—original draft (lead); writing—review and editing (lead).

## Data Availability Statement

The data that support the findings of this study are available from the corresponding author upon reasonable request.

## Keywords

metal oxide nanoparticles, microplastics, niobium pentoxide, photocatalysis

Received: February 26, 2025
Revised: April 20, 2025
Published online: May 15, 2025

[1] A. Thacharodi, S. Hassan, R. Meenatchi, M. A. Bhat, N. Hussain, J. Arockiaraj, H. H. Ngo, A. Sharma, H. T. Nguyen, A. Pugazhendhi, *J. Environ. Manage.* **2024**, *351*, 119988.
[2] Y. Zhu, R. Che, X. Zong, J. Wang, J. Li, C. Zhang, F. Wang, *J. Environ. Manage.* **2024**, *352*, 120039.
[3] J. Chen, J. Wu, P. C. Sherrell, J. Chen, H. Wang, W. X. Zhang, J. Yang, *Adv. Sci.* **2022**, *9*, 2103764.
[4] G. Zhou, H. Xu, H. Song, J. Yi, X. Wang, Z. Chen, X. Zhu, *ACS Catal.* **2024**, *14*, 8694.
[5] S. Chu, B. Zhang, X. Zhao, H. S. Soo, F. Wang, R. Xiao, H. Zhang, *Adv. Energy Mater.* **2022**, *12*, 2200435.
[6] S. H. Paiman, S. F. Noor, N. Md Ngadi, A. H. Nordin, N. Abdullah, *Chem. Eng. J.* **2023**, *467*, 143534.
[7] J. Y. Kim, D. H. Youn, *Molecules* **2023**, *28*, 6502.
[8] G. C. Assis, R. Antonelli, A. O. S. Dantas, A. C. S. C. Teixeira, *J. Env. Chem. Eng.* **2023**, *11*, 111107.
[9] W. Li, W. Zhao, H. Zhu, Z. J. Li, W. Wang, *J. Mater. Chem. A* **2023**, *11*, 2503.
[10] J. He, L. Han, W. Ma, L. Chen, C. Ma, C. Xu, Z. Yang, *iScience* **2023**, *26*, 106833.
[11] J. Liu, D. Zhao, X. Wu, D. Wu, N. Su, Y. Wang, F. Chen, C. Fu, J. Wang, Q. Zhang, *J. Mater. Chem. A* **2025**, *13*, 4429.
[12] I. Nabi, A. U. Bacha, K. Li, H. Cheng, T. Wang, Y. Liu, S. Ajmal, Y. Yang, Y. Feng, L. Zhang, *iScience* **2020**, *23*, 101326.
[13] D. Wang, P. Zhang, M. Yan, L. Jin, X. Du, Z. Fan, Q. Wang, B. Ni, C. Chen, *Polym. Degrad. Stab.* **2022**, *195*, 109806.
[14] Y. He, A. U. Rehman, M. Xu, C. A. Not, A. M. C. Ng, A. B. Djurišić, *Heliyon* **2023**, *9*, e22562.
[15] X. Jiao, K. Zheng, Q. Chen, X. Li, Y. Li, W. Shao, J. Xu, J. Zhu, Y. Pan, Y. Sun, Y. Xie, *Angew. Chem., Int. Ed.* **2020**, *59*, 15497.
[16] J. Jeyaraj, V. Baskaralingam, T. Stalin, I. Muthuvel, *Environ. Res.* **2023**, *233*, 116366.
[17] M. C. Ariza-Tarazona, J. F. Villarreal-Chiu, J. M. Hernández-López, J. R. De la Rosa, V. Barbieri, C. Siligardi, E. I. Cedillo-González, *J. Hazard. Mater.* **2020**, *395*, 122632.
[18] A. D. Vital-Grappin, M. C. Ariza-Tarazona, V. M. Luna-Hernández, J. F. Villarreal-Chiu, J. M. Hernández-López, C. Siligardi, E. I. Cedillo-González, *Polymers* **2021**, *13*, 999.
[19] B. E. Llorente-García, J. M. Hernández-López, A. A. Zaldívar-Cadena, C. Siligardi, E. I. Cedillo-González, *Coatings* **2020**, *15*, 658.
[20] M. Saifuddin, Y. Ghaffari, S. Y. Park, C. G. Kim, *Environ. Res.* **2022**, *212*, 113422.
[21] M. C. Ariza-Tarazona, C. Siligardi, H. A. Carreón-López, J. E. Valdéz-Cerda, P. Pozzi, G. Kaushik, J. F. Villarreal-Chiu, E. I. Cedillo-González, *Mar. Pollut. Bull.* **2023**, *193*, 115206.
[22] P. Chattopadhyay, M. C. Ariza-Tarazona, E. I. Cedillo-González, C. Siligardi, J. Simmchen, *Nanoscale* **2023**, *268*, 14774.

[23] P. Kaewkam, A. Kanchanapaetnukul, J. Khamyan, N. Phadmanee, K. Y. A. Lin, K. Kobwittaya, S. Sirivithayapakorn, *J. Environ. Chem. Eng.* **2022**, *10*, 108131.
[24] X. Zhao, Z. Li, Y. Chen, L. Shi, Y. Zhu, *J. Mol. Catal. A* **2007**, *268*, 101.
[25] S. Y. Tan, W. C. Chong, S. Sethupathi, Y. L. Pang, L. C. Sim, E. Mahmoudi, *Chem. Eng. Res. Design* **2023**, *190*, 550.
[26] J. Shao, K. Deng, L. Chen, C. Guo, C. Zhao, J. Cui, T. Shen, K. Li, J. Liu, C. Fu, *Green Process. Synth.* **2021**, *10*, 499.
[27] C. Venkataramana, S. M. Botsa, P. Shyamala, R. Muralikrishna, *Chemosphere* **2021**, *265*, 129021.
[28] K. Su, H. Liu, Z. Gao, P. Fornasiero, F. Wang, *Adv. Sci.* **2021**, *8*, 2003156,
[29] K. Singh, S. Abhimanyu, S. Sonu, V. Chaudhary, P. Raizada, S. Rustagi, P. Singh, P. Thakur, V. Kumar, A. Kaushik , *Adv. Colloid Interface Sci.* **2024**, *332*, 103273,
[30] C. Zhou, R. Shi, G. Yang, X. Meng, L. Z. Wu, C. H. Tung, T. Zhang, *Mater. Today Chem.* **2018**, *10*, 259.
[31] J. Wang, C. Zhou, J. Wu, T. Zhang, *J. Mater. Chem. A* **2024**, *12*, 4123.
[32] X. Liu, R. Zheng, R. Yuan, L. Peng, Y. Liu, J. Lin, *Sci. Tech.* **2017**, *6*, P665.
[33] N. Suzuki, T. Athar, Y. T. Huang, K. Shimasaki, N. Miyamoto, Y. Yamauchi, *J. Ceram. Soc. Jpn.* **2011**, *119*, 405.
[34] R. Shao, Z. Cao, Y. Xiao, H. Dong, W. He, Y. Gao, J. Liu, *RSC Adv.* **2014**, *4*, 26447.
[35] S. Qi, R. Zuo, Y. Liu, Y. Wang, *Mater. Res. Bull.* **2013**, *48*, 1213.
[36] C. Jaramillo-Páez, F. J. Sánchez-Fernández, J. A. Navío, M. C. Hidalgo, *J. Photochem. Photobiol. A* **2018**, *359*, 40.
[37] H. Liu, N. Gao, M. Liao, X. Fang, *Sci. Rep.* **2015**, *5*, 7716.
[38] N. Kumari, K. Gaurav, S. K. Samdarshi, A. S. Bhattacharyya, S. Paul, B. Rajbongshi, K. Mohanty, *Sol. Energy Mater. Sol. Cells* **2020**, *208*, 110408.
[39] T. Košutová, L. Horák, P. Pleskunov, J. Hanuš, D. Nikitin, P. Kúš , M. Cieslar, I. Gordeev, S. Burazer, A. Choukorov, M. Dopita, *Mat. Chem. Phys.* **2022**, *277*, 125466.
[40] R. Gruehen, *Metals* **1966**, *11*, 119.
[41] T. S. Ercit, *Mineral. Petrol.* **1991**, *43*, 217.
[42] G. H. M. Gomes, N. D. S. Mohallem, *Mater. Lett.* **2022**, *318*, 132136.
[43] S. Yun, Y. Si, J. Shi, T. Zhang, Y. Hou, H. Liu, S. Meng, A. Hagfeldt, *Sol. RRL* **2020**, *4*, 1900430.
[44] C. Nico, T. Monteiro, M. P. F. Graça, *Prog. Mater. Sci.* **2016**, *80*, 1.
[45] J. Xu, X. Jiao, K. Zheng, W. Shao, S. Zhu, X. Li, J. Zhu, Y. Pan, Y. Sun, Y. Xie, *Natl. Sci. Rev.* **2022**, *9*, nwac011.
[46] L. A. Ningsih, P. Y. Lu, S. Ashimura, M. Yoshida, W. C. Chen, Y. C. Chiu, C. Hu, *Chem. Eng. J.* **2024**, *480*, 148089.
[47] N. H. E. Ho, C. Not, *Environ. Pollut.* **2019**, *245*, 702.
[48] J. Masura, J. E. Baker, G. D. Foster, C. Arthur, C. Herring, Laboratory methods for the analysis of microplastics in the marine environment: recommendations for quantifying synthetic particles in waters and sediments, NOAA Technical Memorandum NOS-OR&R-48 **2015**, https://repository.library.noaa.gov/view/noaa/10296 (accessed: April 2025).